15 Chemical Dynamics in Clusters

Jack A. Syage

15.1 Introduction

Research involving clusters is changing the way in which scientists view properties of matter. Clusters exhibit properties that are intermediate between gas-phase and bulk-phase and, as a result, are providing unique insight into these conventional phases of matter. Not surprisingly, cluster research is being pursued in a wide variety of scientific disciplines, including atomic physics (condensation, electron shell structure), laser physics (excimers), material science (crystal growth, phase transitions), chemistry (microsolvation, catalysis), and biochemistry (site-selective bonding, enzyme activity) [1, 2]. Our particular interest is in chemical reactivity in clusters and the dynamical events (e.g., energy redistribution, bond rearrangement, solvent reorganization) that accompany chemistry. The focus in this review will be on two systems:

(1) excited-state proton transfer involving phenol bound to small clusters of solvent molecules, and
(2) radical reactions involving energetic CH_3 radicals in $(CH_3I)_n$ clusters. In both studies, chemistry is initiated by a pump pulse, and reactant and products are detected by a probe pulse by photoionization. The reactions occur on a picosecond timescale.

Time-resolved studies of cluster chemistry can be traced back to the work of Felker and Zewail, who measured the picosecond dynamics of hydrogen-bond dissociation for the stepwise solvation of isoquinoline [3]. Several groups are now investigating real-time dynamics in clusters [3–19] (see also Chapters 2 and 12–14). A number of these efforts involve excited-state proton transfer [6, 14–19], which is the major subject of this account. The Zewail group first reported on the 1-naphthol–ammonia system and observed a distinct threshold to reaction at the level of three ammonia solvent molecules [6]. This result was corroborated by Kelley, and Bernstein, and coworkers [14]. In a related series of experiments Brucker and Kelley measured proton-transfer rates in small solvent complexes formed in cryogenic argon matrices [20]. They observed similar solvent-size dependences for 1-naphthol–ammonia; however, the rates differed from those of the isolated clusters formed in molecular beams, presumably because of the polarizability of the Ar matrix.

The methodology of ultrafast studies of clusters has been applied to other types of reactions. Considerable effort has been directed to the problem of dissocation and cage recombination in I_2^- by Lineberger's group [7] and in I_2 by Zewail's group [5] (see also Chapter 2). The Zewail group has also made detailed measurements of dissociation of rare-gas and H_2 solvent molecules X in small $I_2 \cdot X_n$ clusters [4]. Recently Castleman and coworkers measured femtosecond reaction dynamics for excitation to the dissociative $\tilde{A}$ state in ammonia clusters [13] (see also Chapter 14). A growing body of literature is also concerned with the time evolution of van der Waals dimer dissociations [8–10].

The driving force for most condensed-phase chemistry is solvation, which we define as the static and dynamic interactions that alter the energy states of a reactive solute molecule and that stabilize product. These interactions may be grouped into an additive contribution, representing the individual solvent–solute interactions, and a cooperative contribution, where solvent–solvent interactions affect the solute static and dynamic energy level structure. The cooperative interactions are expected to be particularly important for strongly bound solvents (e.g., hydrogen-bonding molecules). The dependence of solution-phase chemistry on macroscopic bulk-phase properties of solvents is well known and successfully described by empirical models and continuum theories [21–23]. Much less is known about the detailed microscopic processes governed by pairwise molecular interactions and local dynamics.

The theme of this review is the study of clusters as a model of molecular-level solvation. The production of size-specific clusters represents an ideal medium for studying solvent–solute interactions on a single-molecule basis and for allowing systematic control in determining how these interactions are modified by the stepwise addition of solvent molecules. Experimental methods are now well established for controlling important properties of clusters, making them ideally suited for molecular-level studies of solvation. For example:

(1) It is possible to measure properties of individual cluster sizes by optically selective excitation and mass-resolved detection. A series of measurements as a function of cluster size provides direct information on how properties such as reactivity, electronic-state energies, energy and structural relaxation are influenced by addition of single molecules.
(2) Because the internal energy of the clusters can be made low relative to the photoexcitation energy, the excited-state clusters are essentially isoenergetic and constitute a microcanonical ensemble (i.e., an ensemble of noninteracting subsystems at constant energy). Thermal averaging effects are minimized in photochemical cluster studies.
(3) The specific cluster size, composition (e.g., when using mixed solvents), and geometry are often known, making it possible to explore specific structural and solvent–core effects that would otherwise be averaged out in condensed-phase studies. Elegant cluster spectroscopy and dynamics experiments are providing important structural information for interpreting dynamical measurements [24–27].
(4) Experimental results for finite and discrete cluster solvents are more amenable to molecular-level or quantum-level theoretical modeling than are bulk-phase results.

These advantages of clusters provide an interesting vantage point for learning about molecular-level interactions under pseudo-bulk-phase conditions.

15.2 Experimental Methods

15.2.1 Molecular Beam Mass Spectrometry and Photoelectron Spectroscopy

The most common method of producing clusters is by supersonic expansion. This process gives rise to molecular cooling and low-energy collisions that promote cluster growth [28]. The cold clusters are formed nearly exclusively in their vibrationless level with rotational energy that is negligible on a chemical-energy scale. Photoexcitation energy accounts for a large fraction of the total cluster internal energy. We employ photoionization mass spectrometry and photoelectron spectroscopy in our work. These capabilities are described below.

The molecular beam time-of-flight (TOF) mass spectrometer (MS) system pictured in Fig. 15.1 a is our most frequently used apparatus for clusters work. It employs a temperature-controlled pulsed valve that can be positioned along three axes during experiments. The free-jet expansion is skimmed and the resulting collimated beam is passed through a set of TOF ion optics. The molecular beam and TOF axes are indicated in Fig. 15.1 a. The laser beam crosses orthogonally at the intersection of these two axes. The parallel grids comprising the TOF ion optics are separated by 1 cm and the flight tube length is 1 m. Routine mass resolution $m/\Delta m$ is about 200. Three types of experiments are conducted in this apparatus. Multiphoton ionization is used for time-resolved measurements by picosecond pump–probe excitation [15–19] and for spectroscopic measurements by nanosecond excitation. Electron-impact (EI) ionization is used to measure ionization cross sections in noncluster experiments [29–31], to monitor cluster distributions as a function of pulsed valve conditions, and to measure thermochemical thresholds for cluster ion fragments. Finally, a combination of EI ionization, mass filtering, and laser photodissociation is used to measure size-specific electronic spectra and fragmentation mechanisms of cluster ions [32, 33].

Molecular beam photoelectron spectroscopy (PES) is carried out in an apparatus shown in Fig. 15.1 b. This device uses a paraboloidal electrostatic reflector (PER) to increase the collection efficiency of electrons detected by TOF energy analyzers [16 c, 17, 34, 35]. This feature is crucial for studies using low-energy laser pulses (e. g., in ultrafast spectroscopy) and for clusters where the density of any particular cluster size in the molecular beam can be very low. Laser pulses cross the molecular beam perpendicularly by passing through holes drilled in the side of the paraboloidal grids. The chamber containing the pulsed valve also includes ion acceleration optics and a reflectron device for recording ion mass spectra. Because PES does not distinguish between electrons originating from different cluster masses, it is important to choose systems that have well characterized cluster spectroscopy so that specific cluster sizes

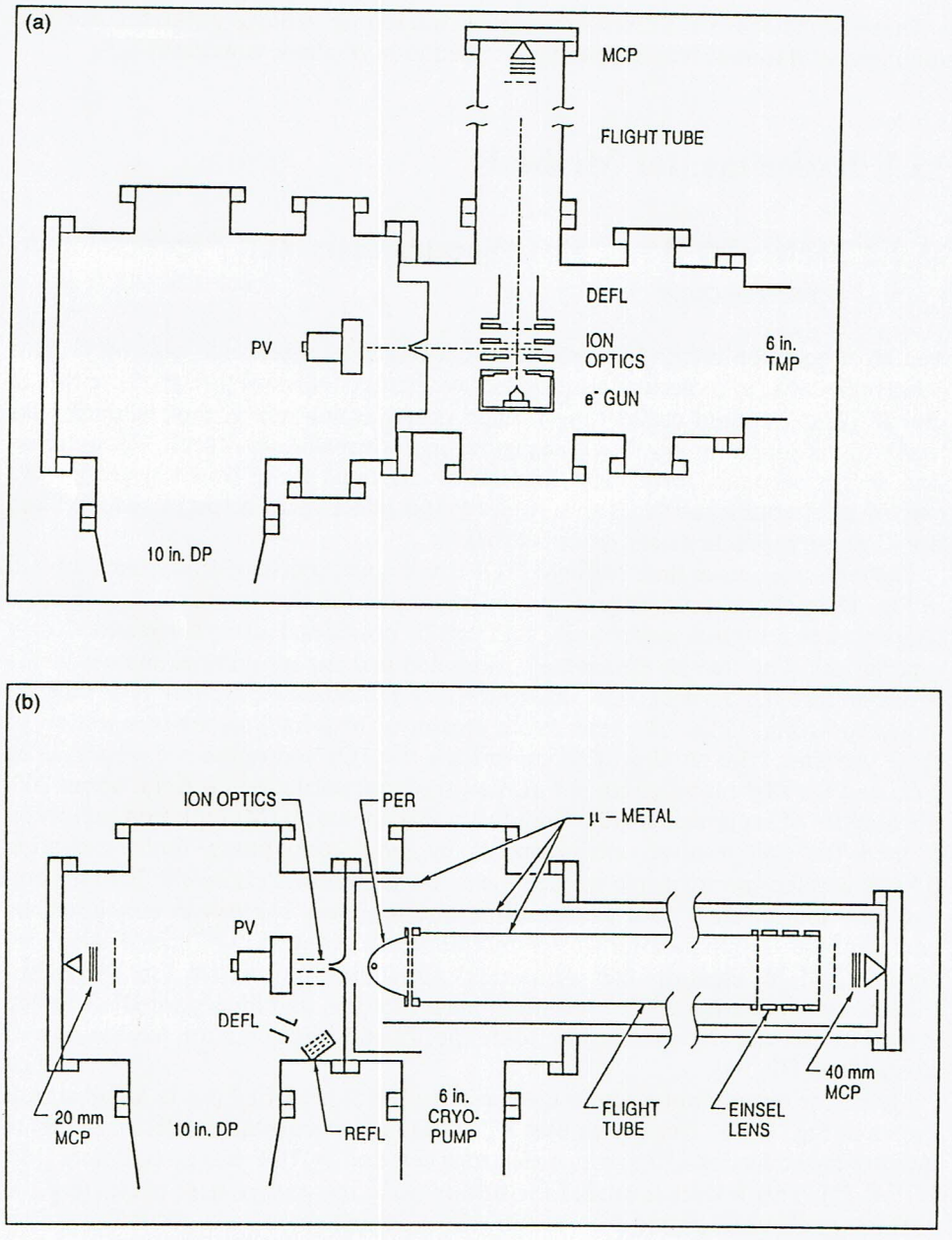

Figure 15.1 Experimental schematic: (a) molecular beam mass spectrometer, (b) molecular beam photoelectron spectrometer. Terms are defined as follows: DEFL, deflector plates; DP, diffusion pump; MCP, microchannel plate detector; PER, paraboloidal electrostatic reflector; PV, pulsed valve; REFL, reflecting grids; TMP, turbomolecular pump. The laser beam crosses orthogonally with the molecular beam at the intersection with the flight tube axis in (a), and through holes in the side of the PER in (b).

can be selected by optical excitation. Alternatively, we have some capacity for detecting mass-selective PES spectra by simultaneously recording ion mass spectra (chamber I) and PES spectra (chamber II). Pulsed-valve and excitation conditions can be adjusted to enhance or discriminate against certain cluster sizes and these changes in the mass spectrum can be correlated with changes in the photoelectron spectrum.

The cluster samples were prepared by a variety of procedures. Solid compounds, such as phenol, were placed in a sample holder in the pulsed valve and heated to 40–60 °C. For ammonia solvation, a 2-liter high-pressure cylinder was made up containing 1–10% ammonia in helium or argon. Water and methanol solvation was achieved by flowing helium through a bubbler containing either of these solvents. The CH_3I samples were prepared by flowing Ar (100–200 kPa or better to say 1–2 atm) through a bubbler that was cooled in a bath of dry ice/$CHCl_3$ (−63 °C), dry ice/CCl_4 (−23 °C), or ice water, depending on the extent of clustering desired.

15.2.2 Excitation and Detection

The chemistry that we will discuss is initiated by a photoexcitation pulse and the evolution of cluster properties are interrogated at later times by various probe excitation and detection techniques. A number of possible choices for the pump and probe pulses are available from the Nd:YAG harmonics and the dye laser (the latter employs the usual wavelength extension capabilities e.g., doubling, mixing, Raman shifting). Two readily available and frequently used pump–probe arrangements are shown in Fig. 15.2. One arrangement uses the Nd:YAG harmonics, 266 nm as the pump and 532 nm (or 355 nm) as the probe. The other arrangment uses tunable UV output from the dye laser as the pump and 355 nm as the probe. We employ other combinations on occasion for both cluster and noncluster work (i.e., 266 + Vis, UV + 532, UV + Vis). The Nd:YAG laser has a pulsed rather than a continuous mode-locked oscillator. A single pulse from the pulse train is extracted and amplified. Pulse characteristics at the fundamental 1064 nm wavelength are 30 ps duration, 70 mJ energy, and 10 Hz repetition. The Nd:YAG second harmonic at 532 nm is used to pump the tunable dye laser oscillator and amplifiers. The oscillator yields tunable pulses of several nanojoules that pass through four stages of dye amplification to give 1–2 mJ pulses of 5–10 ps duration.

All chemistry discussed here was initiated using single-photon excitation in the UV. Probe ionization was achieved using single-photon and multiphoton excitation. In some instances, it was advantageous to use high ionization energy to dissociate the resulting cluster ions. This is the case when reactant and product clusters are of the same mass (e.g., in proton transfer) and not easily distinguishable by mass spectrometry unless they have different propensities for dissociating as ions.

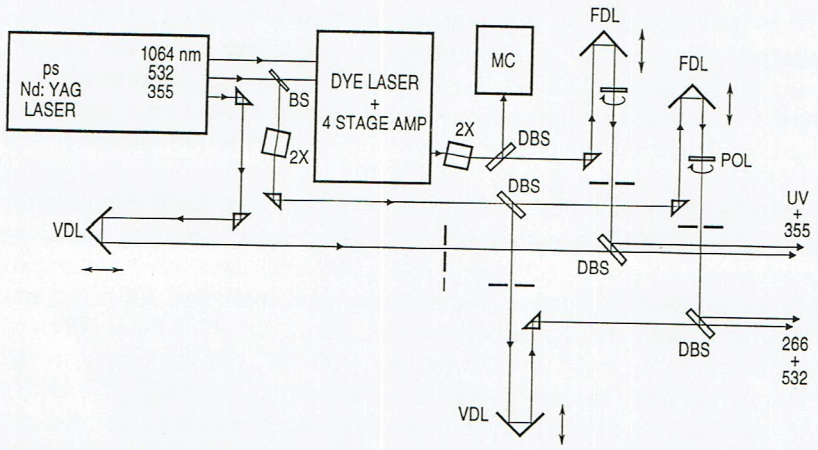

Figure 15.2 Optical layout. Terms are defined as follows: BS, beam splitter; DBS, dichroic beam splitter; FDL, fixed delay line; I, iris; MC, monochromator; POL, polarization rotator, VDL, variable delay line, 2X, doubling crystal.

15.3 Excited-State Proton Transfer

Few phenomena play as prominent a role in the course of nature as hydrogen bonding and proton transfer [36]. Biological roles are numerous. Hydrogen bonding is the cornerstone to genetic replication through DNA base pairing. Furthermore, photoinduced excited-state proton transfer (ESPT) has been implicated as a mechanism of transcription error that can lead to loss of genetic information [37]. The very specific nature of hydrogen bonding and proton transfer also largely accounts for the selectivity of enzyme catalysis in proteins. In laboratory synthetic chemistry, acid and base conditions are often used to catalyze specific reaction pathways.

Aromatic alcohols are known to be more acidic in their S_1 state than in S_0 (the so-called pH jump) [38]. These reactions have been studied extensively in the condensed phase, including several time-resolved experiments [38–40]. Cheshnovsky and Leutwyler were the first to study ESPT in clusters by investigating the system 1-naphthol–$(NH_3)_n$ [41]. The steady-state mass spectra and emission spectra they recorded using nanosecond excitation indicated a cluster size threshold for reaction of $n = 4$. Solgadi *et al.* measured steady-state threshold ionization curves for phenol–$(NH_3)_n$ and also reported an ESPT threshold of $n = 4$ [42], even though phenol is believed to be a weaker acid than naphthol. We have carried out mass-resolved picosecond measurements of the phenol (PhOH) ESPT reaction. The proton transfer, represented by

$$PhOH^*B_n \xrightarrow[k]{} PhO^{*-}H^+B_n$$

corresponds to a conversion from the locally excited S_1 state of the phenol acid to an excited ion-pair state (B_n refers to the solvent cluster consisting of n molecules of base B). A qualitative picture of the cluster potential energy curves for ground,

excited, and ionic states is given in Fig. 15.3 along with the picosecond pump–probe excitation/detection scheme used to measure the chemical rates. Figure 15.3 also shows representative ion energy distributions, measurable by photoelectron spectroscopy (described in Section 15.3.3). Reactant and product are distinguishable in our experiments by mass spectrometry because they fragment differently upon ionization. Ionization of reactant clusters $PhOH^*\cdots B_n$ produces cluster ions $PhOH^+\cdots B_n$ on the inner potential well where the O–H coordinate is strongly bound. Conversely, ionization of the product ion-pairs $PhO^{*-}\cdots H^+B_n$ produces cluster ions $PhO\cdots H^+B_n$ on the outer well, where facile dissociation occurs to give H^+B_n. The observed reactant and product signals show matching kinetics, which is important for establishing that the observed response is a proton-transfer reaction.

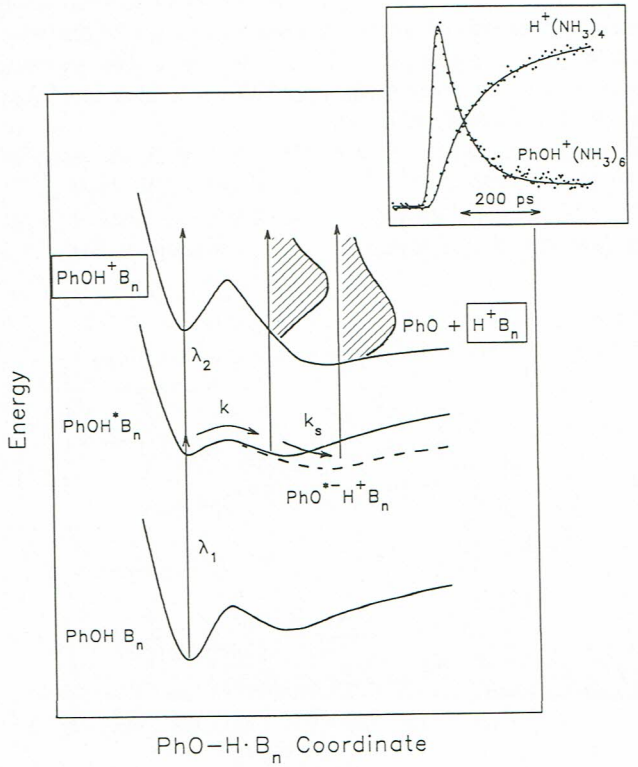

Figure 15.3 Energy diagram for $PhOH(NH_3)_n$ consistent with a cluster size of $n \sim 5$. The pump and probe pulses are denoted as λ_1 and λ_2, and the ESPT and solvent reorganization rate constants are given by k and k_s, respectively. The expected photoelectron band shapes resulting from these processes is also shown (see hatched area). The ion signals for reactant and product are given in the insert and show matching kinetics. A lower n value for the product is plotted to reflect the loss of two NH_3 that evaporate on average in the dissociative ionization step for those specific excitation conditions (266 nm pump, 532 nm probe [15, 18b]).

15.3.1 Stepwise Solvation Properties

We begin by examining the energetics of stepwise solvation. The ion-pair or proton-transfer states in clusters (or condensed phase) are associated with charge-transfer states in gas-phase molecules. Charge-transfer states generally occur at high energy. In phenol, the relevant states are expected to lie at very high energy relative to the covalent S_0 and S_1 states because of the large energy required to form a free proton (the H atom ionization potential is 13.6 eV). Figure 15.4 compares the energy of the covalent S_1 and the correlated excited ion-pair state for small numbers of NH_3 solvent molecules. The ion-pair state, which has large proton character, is stabilized strongly by complexation of phenol to molecules with high proton affinity. The lowering in energy of the ion-pair states by the first solvent molecule is comparable with the proton affinity of the solvent molecule (which is 8.8 eV for NH_3 [43]). Each additional solvent molecule contributes less and less stabilization (the stepwise proton affinity [44]); however, the cumulative stabilization by a few solvent molecules can lower the ion-pair state to energies comparable with that of the S_1 state, thus making ESPT thermodynamically allowed.

Phenol, in a variety of solvent clusters, was excited at 266 nm. The excess energies for NH_3 solvation range from about 1900 cm^{-1} ($n = 1$) to about 2250–2800 cm^{-1} (estimated for $n = 3$–7) [42, 45]. The S_1 origin of uncomplexed phenol is at 274.7 nm [45]. A set of reactant decay measurements are presented in Fig. 15.4

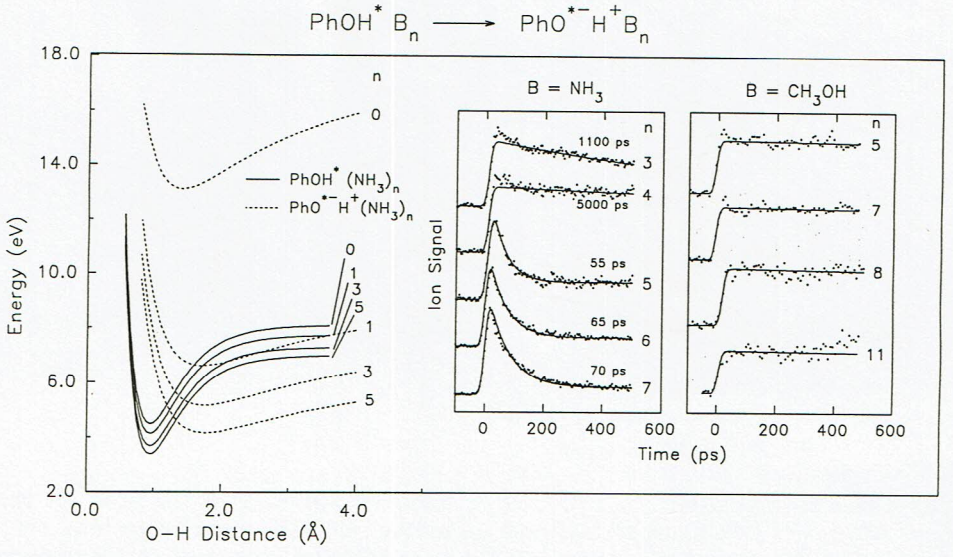

Figure 15.4 Approximate $PhOH(NH_3)_n$ cluster potential energy curves for the reactive PhO–H coordinate. These curves assume an equilibrium O...N bond distance (approximately 1.8 Å and 1.0 Å for the neutral and ion-pair states, respectively). Insert shows observed lifetime of the reactant $PhOH^*B_n$ (as measured by $PhOH^+B_n$ detection) in solvent clusters $(NH_3)_n$ and $(CH_3OH)_n$. The calculated curves are described in [15]. Calculated curves for the $(CH_3OH)_n$ data assume a lifetime of 10 ns.

($\lambda_2 = 532$ nm) as a function of solvent cluster size n for solvents NH_3 and CH_3OH. A distinct threshold for ESPT was observed for NH_3 solvation at $n = 5$. However, no reaction was observed for CH_3OH solvation up to $n = 11$. Results for other solvents are given elsewhere [15]. The observed threshold for NH_3 solvation agrees closely with the simple potential model in Fig. 15.4, lending support to the notion that solvation of high-energy ion-pair states is the mechanism of acid–base chemistry in condensed phase.

If the rates of ESPT for NH_3 solvation in Fig. 15.4 are plotted versus n, the resulting curve takes on a shape and inflection that is reminiscent of an acid–base titration curve. The similarity arises because our mass-specific, time-resolved cluster experiments are, in fact, a it *single-molecule titration measurement.* In similar experiments by Zewail and coworkers [6], and Bernstein, Kelley, and coworkers [14], on 1-naphthol–$(NH_3)_n$, a threshold solvent cluster size of $n = 3$ was observed for ESPT versus $n = 5$ for phenol. The pK_a^* values (i.e., the negative logarithm of the equilibrium constant K_a for acid dissociation) of excited-state 1-naphthol and phenol are 0.5 and 4.1, respectively, which converts to an enthalpy difference of 0.22 eV [46]. Thus, additional ammonia solvent molecules are required to stabilize ESPT in phenol compared with 1-naphthol. Interestingly, time-averaged experiments on 1-naphthol [41] and on phenol [42] in ammonia clusters indicated that both acids exhibit a critical solvent size for ESPT of $n = 4$. These experiments, which provided valuable spectroscopic and dynamic information on ESPT in these clusters, are apparently less suitable than time-resolved experiments for determining the minimum solvent size for inducing ESPT.

15.3.2 Barrier Properties and Tunneling Mechanism

Proton (and electron) transfer reactions are intriguing because they can exhibit quantum-mechanical behavior (in particular barrier tunneling), even in large systems [47–53]. The tunneling probability in condensed-phase systems is strongly dependent on solvent interactions. Static interactions account for the general shape of the potential energy surface and the equilibrium enthalpy of the reaction. Dynamic interactions such as solute–solvent vibrations and fluctuations in solvent orientation and lattice structure modulate the barrier width and the relative energy of the potential wells.

The barrier properties for ESPT are especially interesting in small clusters because it is not known whether a few solvent molecules act in a similar manner to condensed-phase solvents in facilitating tunneling. This raises the question whether tunneling is expected to occur at all in cold clusters and, if so, by what mechanism. We recently investigated this question and obtained evidence that proton tunneling does occur in small clusters of phenol–$(NH_3)_n$ [52]. Hineman *et al.* also reported a tunneling process naphthol–$(NH_3)_n$ clusters [14]. The principal evidence in both studies was the observation that the transfer rate for a deuteron is typically more than an order of magnitude slower than for a proton. A summary of our results for phenol–ammonia clusters is given in Table 15.1. Tunneling probabilities are extremely sensitive to mass, which explains the strong proton/deuteron isotope effect.

Our description of tunneling in excited phenol–ammonia clusters begins with the assertion made earlier that the potential surface and barrier to proton transfer derive from a curve crossing involving a short-range O – H covalent bonding potential and a long-range Coulombic O^-H^+ ion-pair potential (Fig. 15.4) [52, 53]. The potential along the O – H coordinate is represented in Fig. 15.5 a. The example shown is for a fixed O···N distance of 2.8 Å [54] and a fixed solvent coordinate for which the reactant and product energies are isoenergetic. Based on the electronic splitting calculated by Juanós i Timoneda and Hynes for the neutral and ion-pair potentials of a model OH – N complex (1 eV for an O···N distances of 2.8 Å) [49], we obtain a barrier height U_0 of 0.4 eV measured from the vibrationless level. The equilibrium barrier half-width a_0 is estimated to be 0.30 Å [52]. An important point to note is that the barrier width and height depend directly on the O···N distance. Vibrations, such as the symmetric O···N van der Waals stretch mode, will modulate a and U from their equilibrium values, which can lead to enormous enhancements in the tunneling probability during the compression phase of the vibration.

Proton tunneling in clusters has recently been described by two conceptually different models; the first, developed by Hineman *et al.* [14], is based on a bound-to-continuum proton transition and the second, proposed by us [52, 53], is based on a bound-to-bound proton transition (Fig. 15.5) mediated by solvent motion (condensed-phase picture). Both models use Bell tunneling theory and an inverted parabolic barrier [48], integrate over the tunneling modulation caused by the O···N vibration, and obtain good predictions of the proton/deuteron isotope effect. Bell theory assumes that tunneling occurs only when a reactant and product state become degenerate (Fig. 15.5 a). The difference between the two models is in how the density of product states and the probability of having a tunneling resonance are treated. The former model assumes for simplicity a continuum of product states, in which case a tunneling degeneracy exists regardless of reaction free energy. The latter model is more realistic in considering a bound product state, however, this then requires that there be mechanisms for achieving tunneling resonances. This mechanism is solvent motion, which gives rise to fluctuations in the relative energy of the reactant and product states creating momentary degeneracies.

We refer to the solvent configuration in Fig. 15.5 a, for which the reactant and product minimum energies are the same, as $S^{\ddagger}$. The equilibrium solvent geometry, however, will most likely be different for these reactant and product states. Schematic representations of the O – H potential are given in Fig. 15.5 b for equilibrium solvent configurations of the reactant and product, S_r and S_p, respectively. This picture is important because it implies that proton transfer requires solvent motion to reduce the energy of the product state. This condition introduces a solvent activation energy for bringing the reactant and product minimum energies (or vibrationless levels) into resonance [50–53]. A deficiency of the model as it stands is that the energy gaps between reactant and product states can become very large and potentially insurmountable by energy fluctuations due to solvent motion. This predicts that as the reaction free energy becomes more negative (i.e., the driving force increases), reaction rates actually decrease (i.e., the Marcus inverted region). In reality the large energy gaps are reduced by a manifold of product vibrations that can accept energy as a result of proton transfer. Hence, the energy gap that must be overcome by solvent fluctua-

tions is due to the energy separation between product accepting states rather than the reaction free energy [53].

A minimum of four nuclear coordinates are needed to discuss proton tunneling properly: (1) the O−H coordinate q_H, which is the reaction coordinate, (2) the O···N coordinate Q_N, in which the O···N symmetric stretch modulates the internuclear distance between potential minima, which in turn modulates the barrier height and width, (3) the solvent coordinate S, in which solvent modes cause fluctuations in the relative energies of reactant and product, and (4) coordinates corresponding to product accepting modes that reduce the electronic energy gap between reactant and product. All coordinates, except for S, are treated quantally in our model [53].

Calculations of tunneling rates were made as a function of vibrational energy E_{vib}, reaction free energy ΔG_0, and arrier properties such as width and height. A

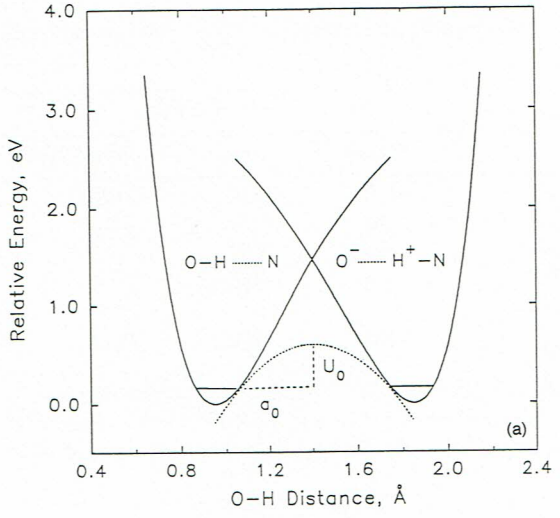

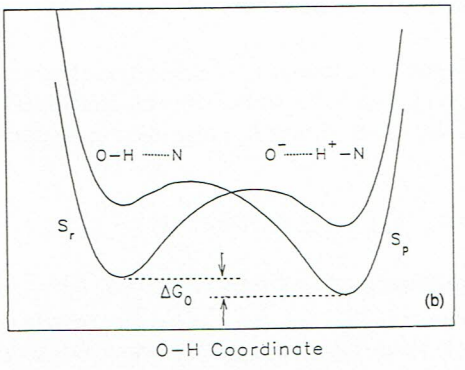

Figure 15.5 (a) Barrier to ESPT arising from the crossing of a covalent and ion-pair potential for $PhOH^*(NH_3)_5$. A parabolic function, used for the tunneling calculations, is fitted to the crossing region; a_0 and U_0 are the barrier half-width and height measured from the vibrationless level of O-H. (b) Schematic representation of the potential energy along the O-H coordinate for fixed solvent configurations S_r and S_p.

summary of calculated and observed rates as functions of size n and, therefore, ΔG_0 is given in Table 15.1. Details of these calculations and comparisons with other experimental parameters are given elsewhere [52, 53]. The three model treatments use the same expressions pertaining to the isotope effect and obtain good agreement with experiment. Where the models differ is as follows:

(1) The bound-continuum model predicts the relative rates as function of E_{vib} well, but cannot handle the rates as a function of ΔG_0.
(2) The solvent-activated bound-bound model is poor to adequate in handling the E_{vib} and ΔG_0 dependence.
(3) The solvent-activated bound-bound model with vibrational coupling, on the other hand, gives reasonable dependences of rate on E_{vib} and ΔG_0.

A better understanding of the effective density of product accepting states will improve the agreement between theory and experiment.

Table 15.1 Comparison of observed and calculated tunneling rates for excited-state phenol-ammonia clusters[a]

	ΔG_0/cm^{-1} [b]	k^{-1}/ps, obs.	k^{-1}/ps, calc.		
			Model I[c]	Model II[c]	Model III[c]
$C_6H_5OH(NH_3)_4$	−2360	5000	470	1350	2700
$C_6H_5OH(NH_3)_5$	−4600	55	42	34	51
$C_6H_5OH(NH_3)_6$	−5640	65	14	63	32
$C_6H_5OH(NH_3)_7$	−6440	70	6	490	58
$C_6H_5OD(ND_3)_5$	−4600[d]	1500	3950[d]	3200	4800
$C_6D_5OD(ND_3)_5$	−4600	2400			

[a] See [52, 53] for details. [b] ΔG_0 values estimated in [53]. [c] Model I = bound-continuum potential; model II = solvent-activated bound-bound potential; model III = model II with product vibrational coupling. [d] Calculations do not differentiate between isotope substituents on the phenol ring.

15.3.3 Solvent Reorganization in Clusters

When proton transfer occurs, the solvent is no longer at equilibrium. The formation of a large product dipole is expected to exert a force on the solvent, leading to further dynamics. For simplicity, we consider that reaction and solvent dynamics are separable, that is

$$PhOH^*\cdots B_n \xrightarrow[k]{} [PhO^{*-}\cdots H^+B_n]_{ur} \xrightarrow[k_s]{} [PhO^{*-}\cdots H^+B_n]_r$$

where the subscripts ur and r denote unrelaxed and relaxed solvent configurations and k_s is the solvent reorganization rate constant (cf. Fig. 15.3). The product formation curves that we recorded show two time-dependences of comparable amplitude,

a rapid rise matching the decay of the $PhOH^+(NH_3)_n$ signals (55–70 ps) and a much slower growth component of about 300 ps [15]. The fast time response is due to the ESPT reaction. The slow time response is ascribed to solvent cluster reorganization.

How the potential energy along the O – H coordinate might change with time due to solvent reorganization is illustrated qualitatively in Fig. 15.3. The solvent network reorganizes to achieve a structure that best accommodates the proton (and counterion). This reorganization or 'solvation of the proton' causes delocalization of charge and lengthening of the O – H bond. The relaxing ion-pair moves closer to a geometry representing the cluster-ion equilibrium configuration. This improves the Franck–Condon (FC) factors for ionization and leads to an increased ionization efficiency with time. The details of this simple kinetic model are given elsewhere [15, 17].

A more definitive measure of geometry change is to monitor individual FC components to ionization. This is achieved by time-resolved photoelectron spectroscopy [17]. In Fig. 15.6a photoelectronic spectra are plotted for different probe delay times. The spectra are broad because of the distribution of cluster sizes, the large density of low-frequency modes, the rapid vibrational redistribution, and the large geometry change upon ionization. The $t = -100$ ps spectrum is identical to the 266 nm-only spectrum (not shown), which arises from ionization of smaller unreactive cluster sizes to form the $PhOH^+(NH_3)_n$ complex (Fig. 15.3). The energy-resolved spectra in Figure 15.6a were obtained by subtracting the strong 266 nm-only signal. (The subtraction was not applied to the time-resolved traces in Fig. 15.6b, therefore, the baseline levels reflect the constant 266 nm-only signal.) For positive t, a low-energy photoelectron band appears. Low-energy electrons correspond to ions with high in

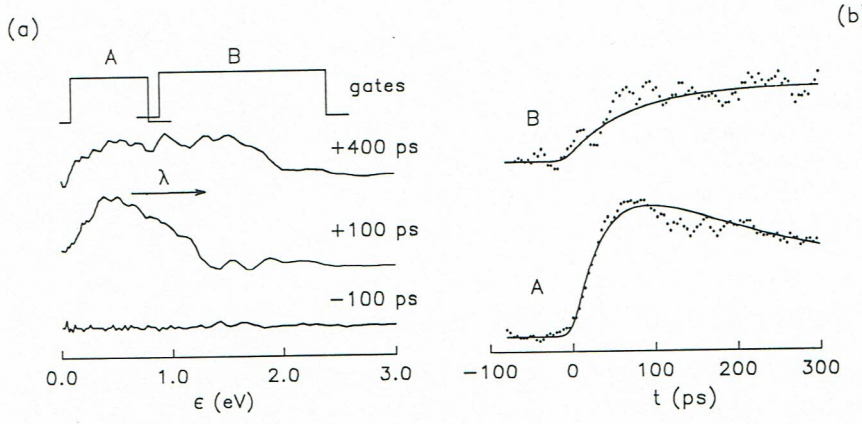

Figure 15.6 Time-resolved photoelectron spectra as a function of pump–probe delay time t. (a) Difference spectra corresponding to $(\lambda_1 + \lambda_2) - (\lambda_1)$. Electrons were accelerated by an additional 2 eV to increase detection efficiency of low-energy electrons. Constant gate widths of 100 ns appear as different widths on the linear energy scale. (b) Observed time-dependences of the low-energy (gate A) and high-energy (gate B) photoelectron bands. Fitted curves were calculated for rate constants $k = (50\ \text{ps})^{-1}$ and $k_s = (300\ \text{ps})^{-1}$ and spectral parameters discussed in [17].

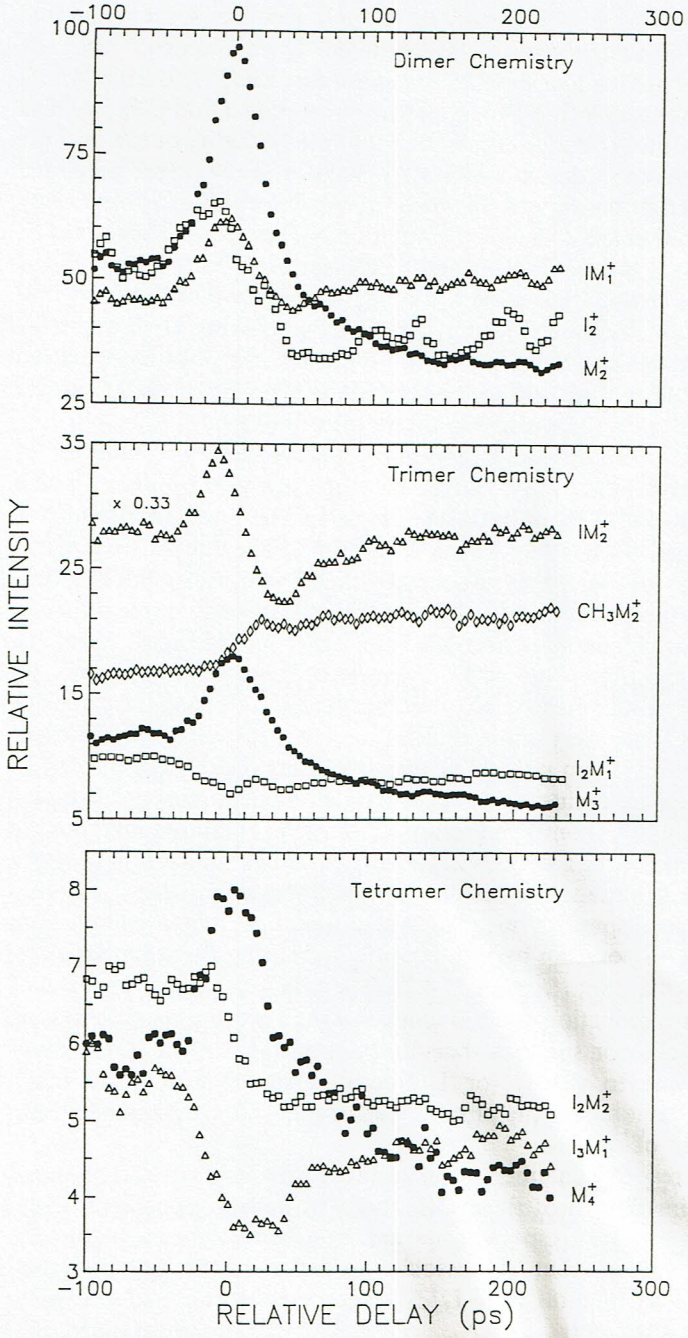

Figure 15.7 Picosecond measurements for photodissociation of M_n clusters ($M = CH_3I$). All traces are plotted on the same relative intensity scale. Note the offset in the ordinate. The time-dependence for loss of one CH_3 (IM_{n-1}, not shown for $n = 4$) is similar to the responses for $n = 2,3$. Excitation was by 266 nm pump and 532 nm probe.

seems to occur. A possible explanation is that these responses reflect a 532 nm ion-photodissociation mechanism. The parent cluster ions M_n^+ are formed with substantial excess energy by three-photon ionization at 266 nm. It is possible that the cluster ions must await vibrational relaxation or nonradiative decay to an absorbing state. Nonradiative decay from the $\tilde{A}$ to the $\tilde{X}$ state of CH_3I^+ is estimated to be on the order of 100 ps [62], which is consistent with the rate observed here. The possibility that the slow components are a neutral reaction channel, however, cannot be ruled out. These features should be studied further.

15.4.2 Explosion in Clusters – Thermal Runaway

The 266 nm picosecond mass spectra in Fig. 15.8 show that the photoexcited clusters can lose a large number of CH_3 groups. Also evident in Fig. 15.8 is an alternation of peak intensities that are separated by two CH_3 mass units. The relative intensities have a dependence on laser pulse energy. The product distribution is observed to shift to greater demethylation at higher pulse energies, so it is likely that sequential photon absorption plays some role in demethylation. However, demethylation is relatively extensive even at low pulse energies (Fig. 15.8 b), indicating that sequential photon absorption cannot account for all the products observed. This conclusion is supported by the photon flux and absorption cross-section data [18].

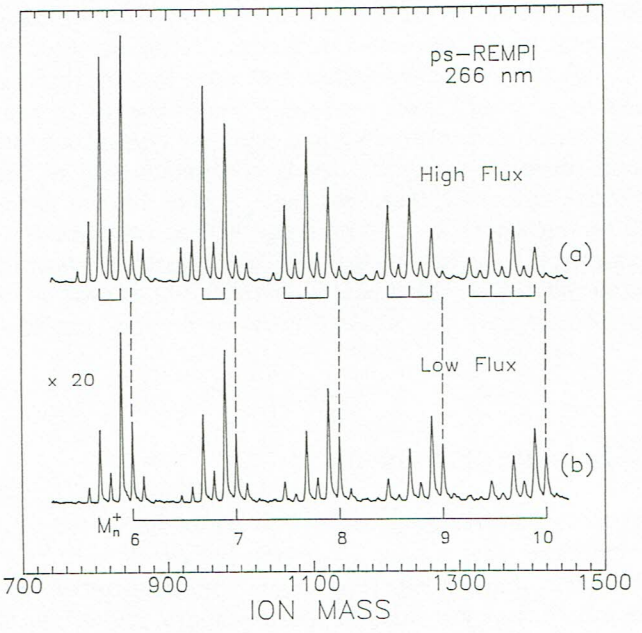

Figure 15.8 Picosecond resonance ionization mass spectra showing reactions in M_n clusters ($M = CH_3I$). The 266 nm high-photon (a) and low-photon (b) flux conditions differ by a factor of about 3 (near 1 GW cm^{-2}). The scaling factor in (b) shows that the overall signal intensity is steeply dependent on photon flux; however, the relative intensities are much less sensitive.

The picosecond measurements and mass spectral features for the small to medium size clusters shown here can be explained by a simple, but not necessarily unique, reaction mechanism based on the chemistry of a 'hot' CH_3 radical. Excitation at 266 nm exceeds the C – I bond energy by about 2.3 eV. The excess energy is released mainly as kinetic energy in the CH_3 radical [63], which can then react as follows:

$$[CH_3 + (CH_3I)_{n-1}] \rightarrow C_2H_6 + I(CH_3I)_{n-2} \qquad \Delta H = -1.37 \text{ eV}$$

where we assume that the photodissociated I atom is lost (recombination of I atoms would contribute an additional exothermicity of $\Delta H = -1.58$ eV). An alternative pathway to production of ethane involves the absorption of two photons by $(CH_3I)_n$ to produce two CH_3 radicals that recombine to release 3.81 eV of heat. In either case, the heat of reaction, augmented by the initial radical kinetic energy and recombination of I atoms, can drive additional chemistry involving exothermic formation of ethane. The hot cluster product above, for example, could undergo the thermal rearrangement

$$I(CH_3I)_{n-2} \rightarrow C_2H_6 + I_3(CH_3I)_{n-4} \qquad \Delta H = -0.52 \text{ eV}$$

The additional heat fuels further loss of ethane. Subsequent photodissociation could also enhance the rate of C–I bond breaking and exothermic production of C_2H_6.

The near-absence of a multiple I atom loss product is consistent with efficient caging of this heavy mass which, because of kinematics (cf. Section 15.4.3), acquires little kinetic energy (0.15–0.25 eV) by photodissociation and even less by thermal decomposition. This provides an efficient means for production of the major product, I_2. Recent work by Ziegler and coworkers [60] and Fan and Donaldson [61] show that on the nanosecond timescale thermally hot I_2 is observed free of the clusters (although the excitation energy and, therefore, the I_2 energy content differ in these two studies). It will be interesting in a future time-resolved experiment to measure the rate of production of I_2 in the cluster and the subsequent rate of evaporation or separation from the cluster. Perhaps I_2 in different vibrational levels will show different time-dependences reflecting some diversity of the local environment in clusters.

15.4.3 Kinetic-Energy Release of I Atoms

Our results show that the chemistry is sufficiently fast for substantial intermolecular chemistry to occur before evaporation. Over time, of course, the cluster does lose constituents. For example, the mass spectra in Fig. 15.8 indicate that extensive methyl loss occurs by way of ethane escape from the cluster. As noted above, iodine loss is limited essentially to a single atom. This observation can be explained by kinematics, in which fragment kinetic energy release (in a two-body system) is inversely proportional to fragment mass. Consequently, I atoms are less likely to escape the cluster and are, therefore, efficiently caged.

It is interesting to compare the properties of I atom loss from $(CH_3I)_n$ clusters with that from bare CH_3I. The latter reaction has been extensively studied by $\tilde{A}$-state excitation and has the properties of a prompt dissociation (<100 fs) [58], namely a large anisotropy in the product angular dependence relative to the laser polarization axis and a large fraction of excess energy released as kinetic energy [63–66]. Figure 15.9 summarizes our measurements of kinetic energy and anisotropy [66]. We present the case for the ground spin orbit state $^2P_{3/2}$ of I, although the same conclusions are reached for the excited $^2P_{1/2}$ state except that less excess energy is available in the latter case for translation.

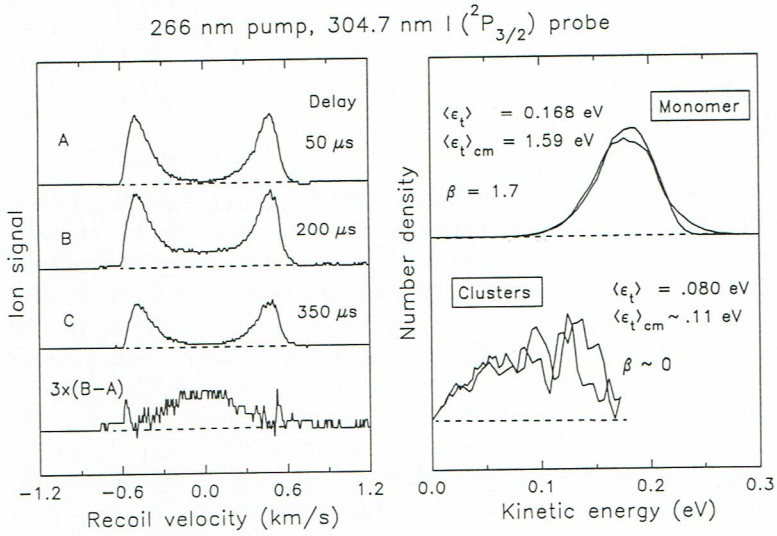

Figure 15.9 Left panel: TOF mass spectra showing I atom recoil from methyl iodide photodissociation. The abscissa has been converted to velocity by the expression $v = q\mathscr{E}\Delta t/m$ where $\mathscr{E}$ is the extraction field and Δt is the displacement in time from the center position. The times in spectra A–C refer to the delay between the laser pulse and the leading edge of a gas pulse which is nominally 400 μs. Right panel: Kinetic energy distribution for CH_3I and $(CH_3I)_n$. The mean center-of-mass kinetic energy $\langle \varepsilon_t \rangle_{cm}$ for clusters assumes an average size of $n = 3$; β is the anisotropy factor. The results for both lobes of the TOF recoil velocity spectra are superimposed on the kinetic energy plots.

Product velocities are measured from the distributions of the ionized product I atoms [66]. The most probable recoil angles for a parallel transition, having the laser polarization aligned along the ion flight tube axis, are toward and away from the detector. The ionized products initially going away from the detector are slowed and turned around by the extraction field, and they arrive at the detector delayed in time with respect to the products initially going toward the detector. The delay is proportional to velocity. All product angles are detected in these experiments, thus the measurement represents the component velocity distribution $P(v_z)$ along the flight tube z-axis (i.e., a one-dimensional projection of a three-dimensional distribution).

The quantity of interest is the number density or fraction of product $f(v)$ with velocity between v and $v + dv$. This function, sometimes referred to as the speed distribution, represents the radial dependence of $P(v)$ [67]. For an isotropic distribution, $f(v)$ is given by

$$f(v)\,dv = P(v)\,4\pi v^2 dv \tag{1}$$

Determination of $f(v)$ from an anisotropic distribution is more complicated and requires a fitting routine. The kinetic energy distributions in Fig. 15.9 are obtained by plotting $f(v)$ versus $mv^2/2$, and mean kinetic energies $\langle \varepsilon_t \rangle$ are obtained from the expression

$$\langle \varepsilon_t \rangle = \frac{m}{2} \frac{\sum v^2 f(v)\,\Delta v}{\sum f(v)\,\Delta v} \tag{2}$$

We recorded TOF spectra for the I atom photofragment for excitation at different times within the gas pulse. The times in traces A–C in Fig. 15.9 refer to the delay between the laser pulse and the leading edge of a gas pulse which is nominally 400-μs. Monomers dominate early and late in the gas pulse because of the lower density of molecules and the warmer expansion temperature, and for the early-time leading edge because the heavier clusters lag behind the monomers in the molecular beam due to slip. It is evident in Fig. 15.9, trace A from the absence of low-velocity component I atoms that dissociation occurs almost exclusively from monomer. Excitation in the middle of the gas pulse, where the formation of clusters is greatest, leads to dissociation of low-energy I atoms. We have extracted an I atom velocity distribution for cluster photodissociation by subtracting spectrum A from B in Fig. 15.9.

The I atom kinetic energy distribution peaks at a much lower value for cluster photodissociation than for that of monomer. This difference is more pronounced when the mean is converted to a center-of-mass kinetic energy by the expression

$$\langle \varepsilon_t \rangle_{cm} = \langle \varepsilon_t \rangle \frac{m_I + m}{m} \tag{3}$$

Because m depends on cluster size and we do not achieve size-specific excitation in this particular experiment, we must assume an average m for the results of the cluster photodissociations. From low-energy EI ionization mass spectra we estimate an average cluster size of $n = 3$. The values of $\langle \varepsilon_t \rangle_{cm}$ reported in Fig. 15.9 are, therefore, based on $m = 15$ amu (CH_3 radical) for monomer and $m = 299$ amu [i.e., $(CH_3I)_2CH_3$ cluster radical] for cluster photodissociation. The anisotropy parameter β is obtained by fitting the angular dependence of the I atom signal to the expression

$$P(\theta) = \frac{1}{4\pi}\left[1 + \frac{\beta}{2}(3\cos^2\theta - 1)\right] \tag{4}$$

where θ is the angle between the laser polarization and flight tube axes. The monomer dissociation is highly aligned along the laser polarization axis and has an anisotropy of $\beta = 1.7$, close to the maximum value of 2, which is consistent with previous investigations [63–65]. This is to be contrasted with the cluster dissociation, which is essentially isotropic ($\beta \sim 0$). The low-energy isotropic distribution of I atoms from clusters is indicative of a dissociation that is not impulsive. Apparently, dissociated I atoms undergo collisions within the clusters that relax much of the initial kinetic energy and delay their escape sufficiently long for rotations to occur. In a sense, I atoms are thermalized in the cluster, some of them recombining to form I_2 and some escaping. Because these experiments probe I atoms and, therefore, do not distinguish specific cluster sizes, it is not yet possible to determine the probability of cage versus escape.

15.5 Conclusions and Outlook

Investigations of chemical properties in clusters are providing unique opportunities to examine solvation and lattice effects on the molecular level and to understand better the correspondence between gas-phase and condensed-phase chemistry. Clusters are uniquely suited for these studies because their size quite naturally spans the limits of the gas phase and the bulk phase, and because their specific composition and geometry are usually fairly well known.

Much of our work is based on proton transfer from the molecule phenol to a hydrogen-bonding solvent cluster. This prototype system has proved valuable in addressing many of the issues above. We observed distinct cluster size thresholds for excited-state proton transfer and explained the results using an energy diagram showing how the excited-state potentials of isolated gas-phase phenol are modified by stepwise addition of solvent molecules. Time-domain measurements are instrumental to our studies. Rate measurements for protiated and deuterated clusters confirmed the tunneling mechanism and helped to establish the barrier properties. Time-resolved photoelectron spectroscopy proved essential for measuring solvent reorganization.

Our studies of photodissociation in $(CH_3I)_n$ clusters yielded many surprises and, consequently, new insight into condensed-phase radical chemistry. The photoinitiation step to generate CH_3 and I radicals was followed by a series of rapid chemistry leading ultimately to the products C_2H_6 and I_2. Interestingly, ethane evaporated extensively from the cluster after reaction, but nearly all of the iodine was caged. Loss of a single I atom was the only significant iodine loss channel. Comparison of measurements of the angle–velocity distribution of I atoms from clusters versus monomer indicate that thermalization precedes dissociation in the former case.

The information gained from cluster studies is beginning to make serious inroads to our understanding of matter. There are broad classes of important chemistry that have not yet been, or are just beginning to be, investigated from the perspective of clusters (photochemical rearrangements, nucleophilic displacements [68],

stereochemistry – to name but a few). Development of new research techniques involving clusters shows no sign of abating. One might expect cluster techniques to be useful for engineering nanotechnologies. Clusters are also ideally suited for studying physical properties of gas–liquid interfaces. It is certain that more applications will evolve and that cluster research will remain fruitful and exciting for the foreseeable future.

Acknowledgements

I am particularly indebted to Jhobe Steadman, who made large contributions to the cluster work reviewed here. These studies were supported by the Aerospace Sponsored Research program.

Final version received: 2nd March 1994.

References

[1] N. Halberstadt, K. C. Janda (Eds), *Dynamics of Polyatomic van der Waals Complexes,* NATO ASI Series, Vol. 227, **1990.**
[2] E. R. Bernstein (Ed.), *Atomic and Molecular Clusters,* Elsevier, New York, **1990**.
[3] P. M. Felker, A. H. Zewail, *Chem. Phys. Lett.* **1983,** *94,* 448, 454.
[4] (a) D. M. Willberg, M. Gutmann, J. J. Breen, A. H. Zewail, *J. Chem. Phys.* **1992,** *96,* 198; (b) M. Gutmann, D. M. Willberg, A. H. Zewail, *ibid.* **1992,** *97,* 8037, 8048.
[5] (a) E. P. Potter, Q. Liu, A. H. Zewail, *Chem. Phys.* **1992,** *200,* 605; (b) Q. Liu, J.-K. Wang, A. H. Zewail, *Nature (London),* **1993,** *364,* 427.
[6] J. J. Breen, L. W. Peng, D. M. Willberg, A. Heikal, P. Cong, A. H. Zewail, *J. Chem. Phys.* **1990,** *92,* 805.
[7] (a) D. Ray, N. E. Levinger, J. M. Papanikolas, W. C. Lineberger, *J. Chem. Phys.* **1989,** *91,* 6533; (b) J. M. Papanikolas, J. R. Gord, N. E. Levinger, D. Ray, V. Vorsa, W. C. Lineberger, *J. Phys. Chem.* **1991,** *95,* 8028.
[8] (a) S. I. Ionov, G. A. Brucker, C. Jaques, L. Velachovic, C. Wittig, *J. Chem. Phys.* **1992,** *97,* 9486; (b) M. P. Cassasa, J. C. Stephenson, D. S. King, *ibid.* **1988,** *89,* 1966; (c) K. Fuke, K. Keizo, F. Misaizu, K. Kaya, *ibid.* **1991,** *95,* 4074.
[9] T. Baumert, C. Röttgermann, C. Rothenfusser, R. Thalweiser, V. Weiss, G. Gerber, *Phys. Rev. Lett.* **1992,** *69,* 1512.
[10] J. L. Knee, L. R. Khundkar, A. H. Zewail, *J. Chem. Phys.* **1987,** *87,* 115.
[11] (a) J. Sipior, M. Sulkes, *J. Chem. Phys.* **1988,** *88,* 6146; (b) C. K. Teh, J. Sipior, M. Sulkes, *J. Phys. Chem.* **1989,** *93,* 5393; (c) S. Arnold, M. Sulkes, *ibid.* **1992,** *96,* 4768.
[12] (a) S. A. Wittmeyer, A. J. Kazishka, M. R. Topp, *Chem. Phys Lett.* **1989,** *154,* 1; (b) A. J. Kazishka, M. I. Shchuka, S. A. Wittmeyer, M. R. Topp, *J. Phys. Chem.* **1991,** *95,* 3663.
[13] S. Wei, J. Purnell, S. A. Buzza, R. J. Stanley, A. W. Castleman Jr, *J. Chem. Phys.* **1992,** *97,* 9480; (b) S. Wei, J. Purnell, S. A. Buzza, A. W. Castleman Jr, *ibid* **1993,** *99,* 755.
[14] M. F. Hineman, G. A. Bruker, D. F. Kelley, E. R. Bernstein, *J. Chem. Phys.* **1992,** *97,* 3341.

[15] (a) J. Steadman, J. A. Syage, *J. Chem. Phys.* **1990,** *92,* 4630; (b) J. A. Syage, J. Steadman, *ibid.* **1991,** *95,* 2497.
[16] (a) J. Steadman, J. A. Syage, *J. Am. Chem. Soc.* **1991,** *113,* 6786; (b) J. Steadman, J. A. Syage, *J. Phys. Chem.* **1991,** *95,* 10326; (c) J. A. Syage, J. Steadman, *ibid.* **1992,** *96,* 9606.
[17] J. A. Syage, *Chem. Phys. Lett.* **1993,** *202,* 227.
[18] (a) J. A. Syage, J. Steadman, *Chem. Phys. Lett.* **1990,** *166,* 159; (b) J. Steadman, E. W. Fournier, J. A. Syage, *Appl. Opt.* **1990,** *29,* 4962.
[19] J. A. Syage, *Ultrafast Spectroscopy in Chemical Systems* (Ed.: J. D. Simon), Kluwer Academic Press, New York, **1994,** p. 289.
[20] (a) G. A. Brucker, D. F. Kelley, *J. Chem. Phys.* **1989,** *90,* 5243; (b) idem., *Chem. Phys. Lett.* **1989,** *136, 213.*
[21] (a) M. Maroncelli, J. MacInnis, G. R. Fleming, *Science* **1989,** *243,* 1674; (b) J. D. Simon, *Acc. Chem. Res.* **1988,** *21,* 128.
[22] (a) I. Rips, J. Klafter, J. Jortner, *J. Chem. Phys.* **1988,** *88,* 3246; (b) M. Sparpaglione, S. Mukamel, *J. Chem. Phys.* **1988,** *88,* 3263; (c) J. N. Onuchic, P. G. Wolynes, *J. Phys. Chem.* **1988,** *92,* 6495.
[23] (a) E. Pines, D. Huppert, N. Agmon, *J. Chem. Phys.* **1988,** *88,* 5620; (b) N. Agmon, D. Huppert, E. Pines, *ibid.* **1988,** *88,* 5631.
[24] (a) L. A. Peteanu, D. H. Levy, *J. Phys. Chem.* **1988,** *92,* 6554; (b) B. B. Champagne, J. F. Pfanstiel, D. F. Plusquellic, D. W. Pratt, W. M. van Herpen, W. L. Meerts, *ibid.* **1990,** *94,* 6.
[25] (a) V. A. Venturo, P. M. Maxton, P. M. Felker, *J. Phys. Chem.* **1992,** *96,* 5234; (b) L. L. Connell, T. C. Corcoran, P. W. Joireman, P. M. Felker, *ibid.* **1990,** *94,* 1229
[26] (a) J. E. Wessel, J. A. Syage, *J. Phys. Chem.* **1990,** *94,* 737; (b) J. A. Syage, J. E. Wessel, *J. Chem. Phys.* **1988,** *89,* 5962.
[27] S. Wei, Z. Shi, A. W. Castleman Jr, *J. Chem. Phys.* **1991,** *94,* 3268.
[28] M. Kappes, S. Leutwyler, in *Atomic and Molecular Beam Methods,* Vol. I (Ed.: G. Scoles), Oxford University Press, New York, **1988,** p. 380.
[29] J. A. Syage, *Phys. Rev. A* **1992,** *46,* 5666.
[30] J. A. Syage, *J. Phys. B.* **1991,** *24,* L527.
[31] J. A. Syage, *J. Chem. Phys.* **1992,** *97,* 6085.
[32] (a) J. A. Syage, *J. Chem. Phys.* **1990,** *92,* 1804; (b) J. A. Syage, J. Steadman, *Rev. Sci. Instrum.* **1990,** *61,* 1204.
[33] J. A. Syage, J. E. Pollard, J. Steadman, *Chem. Phys. Lett.* **1989,** *161,* 103.
[34] J. Steadman, J. A. Syage, *Rev. Sci. Instrum.* **1993,** *64,* 3094.
[35] (a) D. J. Trevor, L. D. Van Woerkom, R. R. Freeman, *Rev. Sci. Instrum.* **1989,** *60,* 1051; (b) G. Liu, J. J. Barton, C. C. Bahr, D. A. Shirley, *Nucl. Instr. Meth.,* **1986,** *A246,* 504.
[36] E. Caldin, V. Gold, *Proton-Transfer Reactions,* John Wiley, New York, **1975.**
[37] O. Löwdin, *Adv. Quantum Chem.* **1966,** *2,* 213.
[38] E. M. Kosower, D. Huppert, *Annu. Rev. Phys. Chem.* **1986,** *37,* 127.
[39] (a) J. Lee, R. D. Griffin, G. W. Robinson, *J. Chem. Phys.* **1985,** *82,* 4920; (b) J. Lee, G. W. Robinson, S. P. Webb, L. A. Philips, J. H. Clark, *J. Am. Chem. Soc.* **1986,** *108,* 6538.
[40] D. H. Huppert, A. Jayaraman, R. G. Maines Sr, D. W. Steyert, P. M. Rentzepis, *J. Chem. Phys.* **1984,** *81,* 5596.
[41] (a) O. Cheshnovsky, S. Leutwyler, *Chem. Phys. Lett.* **1985,** *121,* 1; (b) idem, *J. Chem. Phys.* **1988,** *88,* 4127; (c)T. Droz, R. Knochenmuss, S. Leutwyler, *J. Chem. Phys.* **1990,** *93,* 4520.
[42] (a) D. Solgadi, C. Jouvet, A. Tramer, *J. Phys. Chem.* **1988,** *92,* 3313; (b) C. Jouvet, C. Lardeux-Dedonder, M. Richard-Viard, D. Solgadi, A. Tramer, *ibid.* **1990,** *94,* 5041.
[43] S. G. Lias, J. F. Liebman, R. D. Levin, *J. Phys. Chem. Ref. Data* **1984,** *13,* 695.

[44] (a) P. Kebarle, *Annu. Rev. Phys. Chem.* **1977** *28,* 445; (b) E. P. Grimsrud, P. Kebarle, *J. Am. Chem. Soc.* **1973,** *95,* 7939; (c) M. J. Mautner, C. V. Speller, *J. Phys. Chem.* **1986,** *90,* 6616.
[45] (a) N. Gonohe, H. Abe, N. Mikami, M. Ito, *J. Phys. Chem.* **1985,** *89,* 3642; (b) A. Oikawa, H. Abe, N. Mikami, M. Ito, *ibid.* **1983,** *87,* 5083.
[46] (a) C. M. Harris, B. K. Selinger, *J. Phys. Chem.* **1980,** *84,* 1366; (b) J. F. Ireland, P. A. H. Wyatt, *Adv. Phys. Org. Chem.* **1976,** *12,* 131.
[47] R. M. Rentzepis, P. F. Barbara, *Adv. Chem. Phys.* **1981,** *47,* 627.
[48] R. P. Bell, *The Tunnel Effect in Chemistry,* Chapman-Hall, New York, **1980**, Chapter 2.
[49] J. Juanós i Timoneda, J. T. Hynes, *J. Phys. Chem.* **1991,** *95,* 10431.
[50] (a) D. C. Borgis, S. Lee, J. T. Hynes, *Chem. Phys. Lett.* **1989,** *162* 19; (b) D. C. Borgis, J. T. Hynes, *Chem. Phys.* **1993,** *170* 315; (c) idem., *J. Chem. Phys.* **1991,** *94,* 3619.
[51] (a) R. I. Cukier, M. Morillo, *J. Chem. Phys.* **1990,** *91,* 857; (b) M. Morillo, R. I. Cukier, *ibid.* **1990,** *92,* 4833; (c) N. Makri, W. H. Miller, *ibid.* **1989,** *91,* 4026.
[52] J. A. Syage, *J. Phys. Chem.* **1993,** *97,* 12523.
[53] (a) J. A. Syage, *Faraday Discuss. Chem. Soc.* **1994,** in press; (b) *idem., Proc. SPIE - Int. Soc. Opt. Eng.* **1994,** *2124,* 360.
[54] (a) A. Matsuyama, A. Imamura, *Bull. Chem. Soc. Jpn.* **1972,** *45,* 2196; (b) G. C. Pimentel, A. L. McClellan, *The Hydrogen Bond,* W. H. Freeman, San Francisco, **1960**; (c) D. F. Plusquellic, X.-Q. Tan, D. W. Pratt, *J. Chem. Phys.* **1992,** *96,* 8026; (d) L. L. Connell, Ph.D. Thesis, University of California, Los Angeles, **1992**.
[55] (a) G. Rothenberger, D. K. Negus, R. M. Hochstrasser, *J. Chem. Phys.* **1983,** *79,* 5360; (b) S-G. Su, J. D. Simon, *ibid.* **1988,** *89,* 908.
[56] (a) P. F. Barbara, G. C. Walker, T. P. Smith, *Science,* **1992,** *256,* 975; (b) W. Jarzeba, G. C. Walker, A. E. Johnson, M. A. Kahlow, P. F. Barbara, *J. Phys. Chem.* **1988,** *92,* 7039; (c) M. Kozik, N. Sutin, J. R. Winkler, *Coord. Chem. Rev.* **1990,** *97,* 23.
[57] J. G. Anderson, D. W. Toohey, W. H. Brune, *Science* **1991,** *251,* 39.
[58] J. L. Knee, L. R. Khundkar, A. H. Zewail, *J. Chem. Phys.* **1985,** *83,* 1996.
[59] S. P. Sapers, V. Vaida, R. Naaman, *J. Chem. Phys.* **1988,** *88,* 3638.
[60] P. G. Wang, Y. P. Zhang, C. J. Ruggles, L. D. Ziegler, *J. Chem. Phys.* **1990,** *92,* 2806.
[61] Y. B. Fan, D. J. Donaldson, *J. Phys. Chem.* **1992,** *96,* 19.
[62] S. P. Goss, J. D. Morrison, D. L. Smith, *J. Chem. Phys.* **1981,** *75,* 757.
[63] R. K. Sparks, K. Shobatake, L. R. Carlson, Y. T. Lee, *J. Chem. Phys.* **1981,** *75,* 3838.
[64] (a) M. D. Barry, P. A. Gorry, *Mol. Phys.* **1984,** *52,* 461; (b) G. N. A. van Veen, T. Baller, A. E. de Vries, N. J. A. van Veen, *Chem. Phys.* **1984,** *87,* 405.
[65] (a) R. Ogorzalek Loo, G. E. Hall, H.-P. Haerri, P. L. Houston, *J. Phys. Chem.* **1988,** *92,* 5; (b) S. M. Penn, C. C. Hayden, K. J. Carlson Muyskens, F. F. Crim, *J. Chem. Phys.* **1988,** *89,* 2909.
[66] R. A. Hertz, J. A. Syage, *J. Chem. Phys.* **1994,** *100,* 9265.
[67] W. J. Moore, *Physical Chemistry,* 4th ed., Prentice-Hall, Englewood Cliffs, **1972,** p. 130ff.
[68] (a) D. M. Cyr, G. A. Bishea, M. G. Scarton, M. A. Johnson, *J. Chem. Phys.* **1992,** *97,* 5911; (b) D. M. Cyr, L. A. Posey, G. A. Bishea, C-C. Han, M. A. Johnson, *J. Am. Chem. Soc.* **1991,** *113,* 9697.